

Experimental study of the flow-structure interactions in an air- or helium-filled hard disk drive geometry

S. W. Kil · J. A. C. Humphrey · H. Haj-Hariri

Received: 30 March 2011 / Accepted: 4 November 2011 / Published online: 23 November 2011
© Springer-Verlag 2011

Abstract The increased rotating speed of the hard disk drive (HDD) causes an unsteady flow field between each stack of disks and leads to flow induced vibration on the slider suspension unit (SSU). This flow induced vibration can reduce the positioning accuracy of the SSU and lead to failure to read or write data. Therefore, reduction of turbulence kinetic energy around the SSU is an important step to improve the performance of the HDD. Several modifications have been investigated in air to decrease the direct effect of unsteady flows on the SSU (e.g. spoiler, damper, or divider in the region upstream of the arm). However, these methods are not fundamental solutions for reducing the vibrations on the SSU. Since the HDDs currently in use are filled with air, helium was selected to compare the flow pattern due to the differing inertial property. To visualize the flow pattern, particle image velocimetry (PIV) measurements were performed at the inter-disk mid-plane between a pair of disks near the arm and the SSU. The geometry is an expanded 2× model simulating Seagate cheetah 2.5-inch drive. For both the air and the helium filled drives, measurements have been performed for two different locations of the SSU for two different angular velocities of 1,000 and 3,000 rpm, corresponding to 5,000 and 15,000 rpm in the commercial drive. The results reveal that the flow patterns of the air and the helium flow are quite similar. However, with respect to the turbulence intensity around the SSU, the helium flow shows a drastic

decrease compared with that of the air flow, resulting in much reduced positioning errors. As such, helium-filled drives have merit and should be looked into.

1 Introduction

Ever since the base technologies of hard disk drive (HDD) were invented by Valdemar Poulsen (Wood 2008), the HDD has been widely used for storage of data in computers. Even though many different storage devices (e.g. flash memory, solid state drive, CD, and DVD) are currently in use, the HDD remains the most efficient with the largest capacity of storage. The first HDD was equipped with fifty stacks of disks of 24 inches each, a data storage aerial density of 2 kilobits/in.², and spindle speed of 1,200 rpm. In contrast, today the HDD's are aiming at an aerial density of 0.25 terabits/in.² and rotate at 15,000 rpm (Coughlin 2001). A current hard drive consists of one to five disks. The upper and the lower surfaces of each disk are capable of storing data. One actuator arm is inserted between two disks and two slider suspension units (SSUs) are mounted on the upper and the bottom surface of the actuator arm. At the end of the SSU, a magnetic head, which is facing the surface of the disk, is mounted on the surface of the SSU. As the disk capacity and speed of rotation keep increasing and the disk size keeps decreasing, the data density on a disk surface is constantly increasing. For prompt data transfer from a HDD, the spindle speed has to be increased and the seek time of the magnetic head has to be minimized. To decrease this seek time, strict positioning accuracy of the arm and the SSU has to be maintained. However, the increased rotating speed of the disk induces an unsteady flow in the space between disks. This unsteady and turbulent flow is the main source of

S. W. Kil · J. A. C. Humphrey · H. Haj-Hariri (✉)
Department of Mechanical and Aerospace Engineering,
University of Virginia, 122 Engineer's Way,
P.O. Box 400746, Charlottesville, VA 22904-4746, USA
e-mail: hh2b@virginia.edu

S. W. Kil
e-mail: sk2re@virginia.edu

positioning error of the SSU. Over the years, to decrease the turbulent kinetic energy around the SSU and the actuator arm, several geometrical modifications have been attempted upstream of the SSU and the actuator arm (i.e. an air spoiler, an air dam, an air damping plate and so on). These methods successfully decreased a local velocity magnitude around the SSU and the actuator arm and led to the reduction of the turbulent kinetic energy in the region of interest. However, the presence of the blockage upstream of the actuator arm increased the power consumption of the spindle motor. Therefore, in the present study, helium has been chosen as an alternative medium in the HDD. It is shown that helium due to its higher kinematic viscosity and lower density can effectively stabilize the turbulent kinetic energy around the SSU without raising the power consumption of the spindle motor. The present work concentrates on the comparison of the fundamental physics between the helium flow and the air flow in the same expanded HDD model. The goal was to explore whether there is merit in replacing air of helium. Having shown such merit, the next challenge is that of developing durable seals. The current investigation establishes the first necessary condition for combining helium as the working fluid. It also motivates follow-in studies into the sealing issue.

There have been many studies about the flow pattern between a pair of co-rotating disks with and without obstructions in the middle of the flow field to understand the nature of the flow. Lennemann (1974) visualized the flow pattern between a pair of disks. He observed that the region near the hub rotates at $\sim 80\%$ of the disk speed and that the dented shapes of the laminar core region depended on the shroud to disk spacing distance. Lennemann also reported that the presence of the slider arm could change the flow field completely. The arm induced the vortex sheet downstream of itself which prevented the arm from staying stable.

Abrahamson et al. (1988) submerged glass disks in a water-filled model surrounded by a plexiglass enclosure. They found that the outer region of the disk had more active turbulence than the inner region. Particularly, the space between the shroud wall and the periphery of the disks (shroud boundary region) is the most turbulent of the flow field. Additionally, the existence of a pair of Taylor-Couette-type toroidal vortices was observed near the shroud boundary region.

Tzeng and Humphrey (1991) measured the velocity field on the inter-disk mid-plane between a pair of co-rotating disks with and without the arm by performing laser Doppler anemometry (LDA). They observed that the flow velocity at the tip of the disk is 63% of disk rotating speed for the case without the arm. The velocity field showed that the mean velocity increased corresponding to the increment

of the disk radius. The fluctuation of the velocity increased as it approached the strongly sheared region near the enclosure. Comparing to the result of the unobstructed case, the presence of the arm significantly modified the flow profile from the enclosure wall to the end of the arm. The wake of the arm did not significantly modify the circumferential velocity component in the region downstream to the arm. However, the root mean square (RMS) profile was much affected by the presence of the arm. In the case of unobstructed flow, the maximum fluctuation occurred where the solid body rotation melded into the sheared flow. However, in the obstructed flow, the fluctuations were induced by the sheared flow induced by the arm.

Using a laser Doppler velocimeter (LDV) technique, Usry et al. (1993) obtained the circumferential velocity and corresponding RMS for the flow within a pair of corotating disks enclosed by a cylindrical shroud. Two obstructions geometrically similar with a taper toward the rotating center, but having different lengths were used. The obstructions were inserted in the middle of the flow field one at a time. The result proved that the presence of the obstruction affected the average and time-dependent features of the flow field compared with the unobstructed flow. Particularly, the frequency range of the flow field upstream of the obstruction varied depending on the length of the obstruction, and the strength of the cross-stream secondary-motion was enhanced as the length of the obstruction increased.

Tatewaki et al. (2001) conducted numerical large-eddy simulations (LES) with three disks with and without the obstruction between each stack of the disks. Their results showed that there was the interaction through the clearance between the edge of the disks and the shroud wall for the case of the unobstructed flow. However, the presence of the obstruction effectively removed the interaction between the disks.

Shimizu et al. (2003) simulated the flow field inside the HDD using the LES technique to estimate the aerodynamic force on the Head Gimbal Assembly (HGA). Based on the result of the simulation, the flow induced vibration was estimated by performing a structural analysis. The result showed that the vibration of the HGA was induced by two different mechanisms; vortex-shedding (i) induced by a suspension flange of high and discrete frequency (ii) a low frequency mode induced by the E-block supporting the actuator arm.

Hirono et al. (2004) and Ikegawa et al. (2006) studied the relation between the power consumption of the spindle motor and a spoiler's thickness and length. To measure the vibration of a Head Stack Assembly (HSA), the LDV technique was used with five partially enclosed disks rotating at 10,025 rpm. The result of the experiment showed that the reduction of the flow rate induced by the spoiler

upstream of the arm decreased the flow induced vibration on the HSA. However, the energy loss due to the spoiler increased the power consumption of the spindle motor.

Nakamura et al. (2005) measured the flow induced vibration of the HGA using the LDV technique with various designs of the HGA. They examined three different lengths of the HGA (12, 14.5 and 18 mm). In their investigations, as the length of the HGA reduced, the natural frequency of the HGA became higher. Also, the windage disturbance of 12-mm HGA was 40% less than that of 14.5-mm HGA. Therefore, miniaturization of the HGA was a quite effective way to avoid the windage disturbance.

Barbier et al. (2006) investigated the difference of flow patterns depending on the position of a SSU on an arm. The position of the arm strongly affects the flow in the region downstream of the arm. The authors performed PIV at the inter-disk mid-plane for two different cases. The inner configuration (IC) was the case when the SSU was located near the hub and the outer configuration (OC) was the case when the SSU was close to the rim of the disk. They reported the existence of a three-dimensional reversed flow region near the hub upstream of the arm due to the flow obstruction by the arm. The incoming flow upstream of the arm generated a boundary layer flow on the body of the arm and the SSU and changed direction abruptly at the tip of the SSU. This flow was accelerated and strongly sheared at the tip of the SSU. Moreover, downstream of the arm, three-dimensional vortices were induced by the presence of the arm. These vortices generated a high level of turbulence intensity in the region downstream of the arm and the SSU along the circumferential direction at the inter-disk mid-plane.

Kaneko et al. (2007) investigated the effect of the installation angle between the actuator arm and the incoming flow upstream of the arm. They submerged a tenfold expanded actuator arm in a water tunnel with various installation angles to create a geometrically-similar model to that in air, but at the slower time scale of the motion than the condition in the air. Based on the observations, four different types of vortex shedding from the trailing edge of the arm were detected; (i) Trailing edge vortex with the Strouhal number of 0.24, (ii) Leading edge vortex, (iii) Tip vortex 1 due to the flow wrapping around the tip of the arm, (iv) Tip vortex 2 with small scale vortices.

Kazemi (2008) calculated the flow field in a 3.5-inch commercial HDD rotating at 15,000 rpm to investigate the effect of the fluid force on each component of the HSA. The fluid force was successfully exported from the calculation to perform a finite element method (FEM) analysis. The result revealed that the vortex shedding arising around the HSA had a severe effect on the components of the

HSA, and the frequencies of them were highly related with the vibration of each component in the HSA.

Kazemi (2009) also performed a numerical calculation with a model of 3.5-inch commercial drive rotating at 7,200 rpm to investigate the efficiency of a damping plate upstream of an actuator arm. The result of the calculation revealed that the presence of the damping plate reduced the RMS of the flow field so that the magnitude of the flow induced vibration decreased significantly. Additionally, a weight-saving hole in the middle of the actuator arm induced a vortex structure which resonated with the mode of the HSA between 7 and 9 kHz.

Zhang et al. (2010) investigated an effect of a flow diverter upstream of the actuator arm and a spoiler downstream of the actuator arm. They performed numerical calculations with models of an original commercial drive, a drive with the flow diverter and a drive with the flow diverter and the spoiler. Their results revealed that the presence of those geometrical modifications successfully attenuated the flow induced vibration of the HGA up to 50% of the original model.

While all previous studies have focused on air as the working fluid, Aruga et al. (2007) measured the positioning error signal at the tip of magnetic heads in a helium-filled drive. They compared the result for helium with the result for air. In the experimental apparatus, there were four stacks of disks with diameters of 3.5-inches rotating at 15,000 rpm. The enclosure was completely sealed to prevent a leakage of helium gas. The results were that the helium-filled drive's positioning error was less than half of that for the air-filled drive. Furthermore, low frequency windage, disk flutter, and suspension resonance were reduced by around 10 dB or more in the helium-filled drive.

1.1 Focus of the current work

Prompted by the superior performance of the helium-filled drive mentioned above, PIV measurements have been performed to investigate the differences of the helium-flow and the air-flow in a scaled-up model rotating at 1,000 and 3,000 rpm. Notwithstanding the difficulty with the sealing of helium, the results of the present experiment strongly support that helium can be a good solution to decrease the turbulent kinetic energy around the SSU and the actuator arm, and therefore ensure a higher positioning accuracy of the SSU at higher rotation speeds of the disks. The focus of the work is not only to investigate whether a helium-filled drive is superior to an air-filled one, but also to explore the physical origin of the flow features and interactions that are responsible for such superiority. The latter, to our knowledge, has not been undertaken by other groups.

Having established that helium drives suffer lower positioning errors, and having uncovered the physics which is responsible, the current work can be viewed as the ‘necessary condition’ in deciding whether there is merit in pursuing research into the very real issue of sealing. The substantial advantage of the helium-filled drive shows that research and investment into sealing is worthwhile.

2 Experimental setup

In the current work, PIV measurement technique has been used to visualize the flow field at the inter-disk mid-plane. Since the basic algorithm of the PIV measurement is based on tracing particles dragged by the flow field, the accuracy of measurement is highly related to the tracking of the flow by the particles. In this experiment, particles, a mixture of 20% glycerin and 80% water, were generated by an atomizer (Model 9306 Six-Jet Atomizer from TSI) with a nominal diameter of 1 μm , a density of 123.2 kg/m^3 . Since the flow around the SSU is turbulent, sheared, three-dimensional, and highly time dependent. The sensitivity of a particle to high frequency velocity fluctuation must be estimated. Under the assumption that a particle is spherical and in Stokes’ flow regime, the response time which can be defined by $\tau_p = \rho_p d_p^2 / 18\mu$ (Barbier 2006) is estimated to be 3.96×10^{-12} s for air and 3.75×10^{-12} s for helium. The small time scale of the flow can be estimated by Kolmogorov microscale theory (Davidson 2004). At 3,000 rpm, using the rotating speed at the rim of a disk, the estimated time scale is 2.74×10^{-5} s. Thus, the particle can be assumed to respond instantaneously to the flow.

The shape of the arm and the SSU originated from the Seagate cheetah 2.5-inch commercial drive. Since the SSU in commercial drives has a small thickness, rectangular wide flanges are used to reinforce rigidity along the edges of the SSU. Each SSU is skewed toward its disk (Fig. 1). Since the magnetic head meets the disk surface in commercial drives, this direct contact could possibly create scratches on the transparent disk surface of the experimental disk. Therefore, a slippery material was necessary to be mounted on the SSU.



Fig. 1 Side view of the slider suspension unit

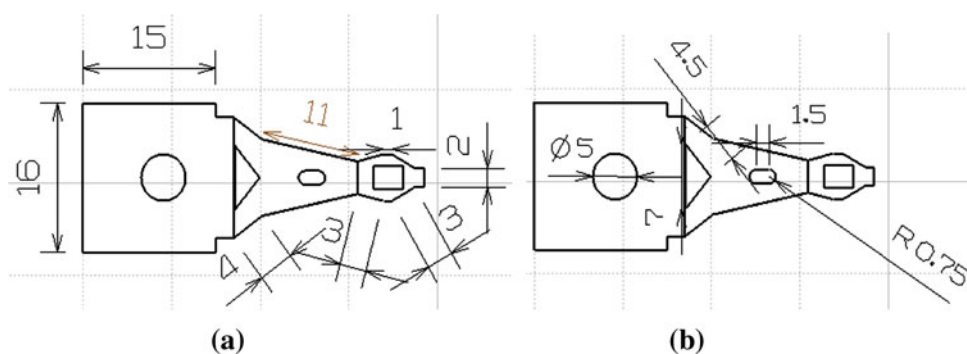
A small Teflon block was chosen as the material to simulate the magnetic head in the experiments (Fig. 2). The shape of the actuator arm was tapered toward the rotating center of the disks, and had two weight-saving holes. The small hole, near the hub, was concentric with a hole in the SSU. The other larger hole had an elliptical shape which was also tapered parallel to the lateral surface of the arm (Fig. 3). Each SSU was mounted on the upper and lower surface facing the disk. To prevent the arm and the SSU from reflecting the laser beam, these components were coated by a black enamel paint (Rust-Oleum enamel, Black, Rust-Oleum corporation). The SSU and the actuator arm was located at the inter-disk mid-plane between a pair of co-rotating disks. The E-block in commercial drives is the component which enables a rotation of the arm. In this experiment, a simulated magnetic block was attached to the E-block to simplify geometries.

A plastic (Plexiglas) enclosure was designed to surround the entire experimental region. Its dimensions are denoted in Fig. 4 and it had a height of 56.35 mm including the thickness of the enclosure wall. Since the PIV measurement acquires data by capturing illuminated particles in a flow field, all surfaces of the enclosure were transparent. Each joint of the enclosure was sealed with an epoxy glue to prevent air or helium from leaking.

PIV Data acquisition is done by capturing images on fluid planes parallel to the disks. Therefore, the upper disk was required to be transparent to capture images on the illuminated plane by the laser beam. Additionally, disks used in the current experiment had to ensure stability at high rotating speed. For this reason, the upper disk was made of glass and manufactured to have a flatness of $\pm 6.35 \times 10^{-3}$ mm. Also, this level of flatness maintained the level of disk wobbling to a maximum of ± 0.07 mm at high rotating speed. Since PIV measurements were concentrated on the

Fig. 2 Dimensions of the slider suspension unit in mm:

a Dimensions **b** Hole size



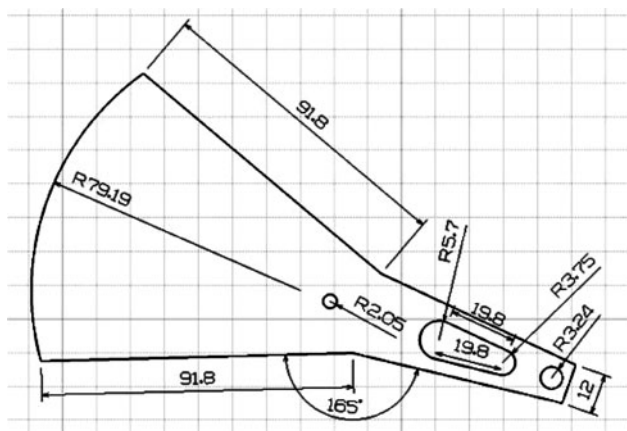


Fig. 3 Top view with the dimensions (mm) of the E-block and the actuator arm

inter-disk mid- plane, the lower disk was designed to have a dark background relative to the plane where images were captured. For this, the lower disk was made of anodized aluminum. The lower disk has the same thickness as the upper disk at its edge. However, it has a thicker inner region on its bottom surface to achieve the reduced level of disk wobbling up of to ± 0.07 mm (Fig. 5). The hub was made of aluminum and its lateral surface was coated by black enamel paint to absorb the laser beam. Due to the difference of inertia between the glass disk and the aluminum hub, there was a possibility that a direct contact between the hub and the disk could create a crack in the glass disk, which would disturb data collection. For this reason, a rubber ring

was inserted between the hub and the upper disk to remove stress concentrations and better distribute the pressure on the upper disk. An aluminum cap was attached to the head of the upper disk to minimize the wobbling of the upper disk. For the same reason as the hub, a rubber ring was inserted between the upper disk and the cap. All dimensions of the components are specified in Table 1.

A DC motor (Reliance, model 1843622004) was installed at the bottom of a rotor which was connected to the lower disk. This motor is able to rotate up to 20,000 rpm. The maximum torque is 1.41 Nm. Since the motor and the rotor could possibly create vibrational noises in the experiment rig, and for safety reasons, an outer steel cylinder to which the motor and rotor were mounted was fixed by a 300 lbs. of concrete to absorb vibrations. Rotating speed was controlled by a single motion axis control PCI card (Galil, DMC 1417) and Galil software (DMC smart terminal). The estimated uncertainty level of the steady rotational speed of motor was less than 1%.

In a real HDD, the magnetic head has to read data at all spots on the disk surface and the displacement of the SSU is parallel to the surface of the disks. For this reason, the arm was designed to rotate parallel to the disk surface. In this experiment, two different configurations were investigated. The inner configuration (IC) corresponds to one third of the full arm stroke from the rotation center. For this case, the center of the Teflon tip was 50.5 mm away from the rotation center. The outer configuration (OC) corresponds to two thirds of the full arm stroke and with the

Fig. 4 Dimensions (mm) of the enclosure

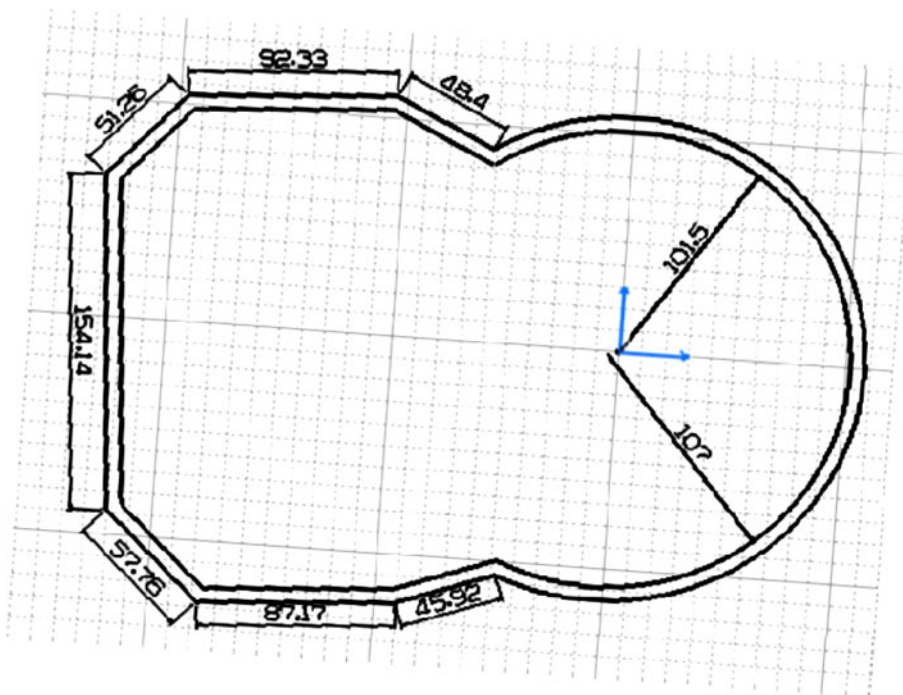


Fig. 5 Schematic drawing of the disks and the hub

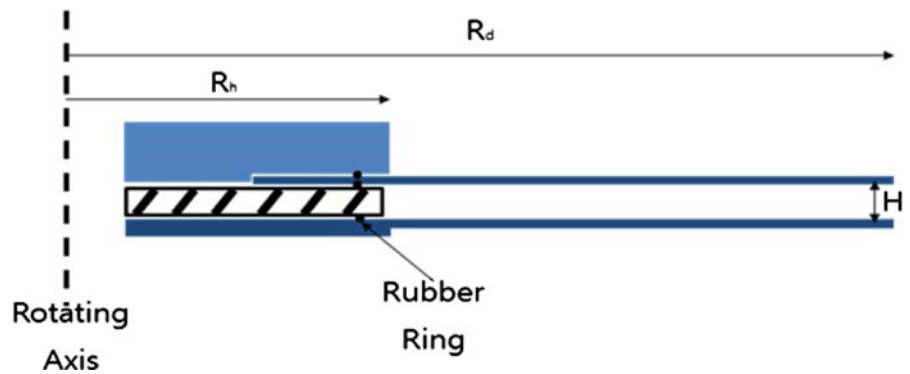


Table 1 Dimensions of disks, hub and rubber ring

Disk radius R_d	100 mm
Hub radius R_h	28.6 mm
Lower disk inner radius R_i	75 mm
Disk thickness T_d	2 mm
Lower disk inner thickness T_i	6.35 mm
Space between disks H	4.8 mm
Height of cap H_c	8 mm
Height of hub H_b	4 mm

center of the Teflon tip had a distance 81.64 mm from the rotation center. Details are illustrated in Fig. 6.

The fluid domain of HDD is geometrically complex. Moreover, due to laser blockage by the presence of blocks and also by connecting edges of the plexiglas walls, PIV measurements were restricted. It takes more than 3 h to complete measurement for one sub-region with 600 image pairs, and 10 Gb of HDD space is required to store 600 image pairs. Therefore, as shown in Fig. 7, eight sub-regions were measured near the arm and the SSU. Each sub-region had the size of $52 \times 52 \text{ mm}^2$ and was divided into 32×32 interrogation windows.

A laser system (New Wave Research Solo PIV III from TSI) was used to perform the PIV. The laser was able to produce a pair of laser beams of wavelength 532 nm, having diameter of 8 mm and energy of 120 mJ per pulse. The time step between two laser pulses and the frequency of the laser beam pair were controlled by a synchronizer (Model LASER PULSE from TSI).

Keane and Adrian (1990) developed the following rules about a time step between pulsed laser beams. (1) one fourth of each interrogation window size is suggested as the maximum in-plane displacements between image pairs. (2) Twice the particle diameter is suggested as the minimum in-plane displacements between image pairs. In this experiment, the sub-domain was divided into 32×32 interrogation windows and the one fourth of interrogation window size is 0.00043 m^2 . Based on these rules, a time

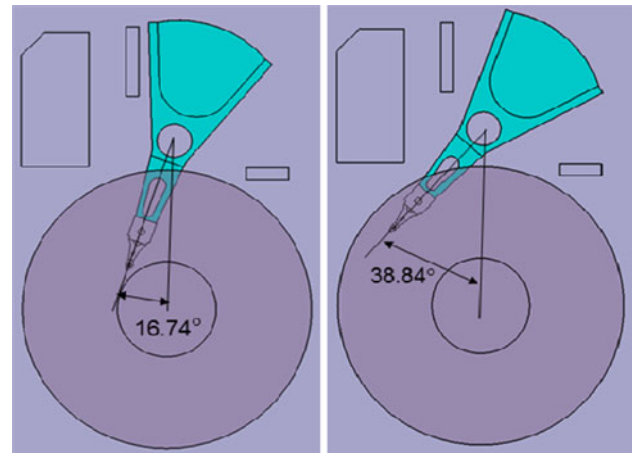


Fig. 6 Schematic drawing of the inner configuration (IC) and outer configuration (OC)

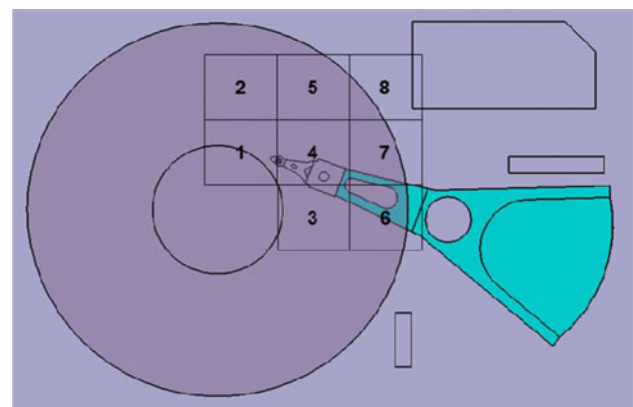


Fig. 7 Schematic drawing of sub-regions for PIV measurement

step of 12 ms was used between sequential pairs of images for the flow field at 1,000 rpm and 4 ms as used at 3,000 rpm. These time steps corresponded to 0.00067% of one disk rotation cycle. For both rotating speeds, the frequency of each laser beam pair was 7.25 Hz. A pulsed laser beam sheet illuminated the plane where PIV measurements were performed.

The laser beam sheet was required to maintain a constant thickness and width to illuminate each sub-region. In this experiment, a spherical lens with 200 mm focal length and a cylindrical lens with −15 mm focal lens were attached at the end of light periscope arm (Light arm. Model 610015 from TSI) which transmitted the laser beam to the test section. The thickness of the laser sheet was estimated to have the value of 0.6 mm.

Image acquisition was processed by a charge coupled device (CCD) camera (Model 630149 Power View PIV from TSI). The CCD camera has 2,048 × 2,048 pixels and a range of 12 bits. The smallest interrogation window size is 32² pixels. Under these conditions, the measurement uncertainty of the camera was estimated to be less than 0.1 pixel. For optimized measurements on the inter-disk mid-plane, a lens with 60 mm focal length was attached to the camera. Since the eight sub-regions were distributed near the arm and the SSU, the CCD camera was mounted on a three-dimensional linear positioner (Model Graduated Knob Unislide A40 series from Velmex, Inc.) which positioned the camera within a tolerance of ±0.001 inch.

3 Results and discussion

All measurement results are obtained on the mid-plane (z = 0 mm) at 1,000 and 3,000 rpm. Mean velocity, V_{mag}^* , turbulence intensity (TI^*) and z-axial vorticity, ω_z^* , are presented. All variables are ensemble averaged with 600 data points and normalized by the tip rotating speed of the disk. The non-dimensionalized values are defined by

$$V_{mag}^* = (U_r^2 + U_\theta^2)^{0.5} / R_d \Omega \tag{1}$$

$$TI^* = (u_r^2 + u_\theta^2)^{0.5} / R_d \Omega \tag{2}$$

$$\omega_z^* = (1/R_d \Omega) (\partial U_\theta / \partial r - \partial U_r / \partial \theta) \tag{3}$$

where * denotes the normalized variables, U_r and U_θ are the radial and circumferential mean velocity components, u_r and u_θ are the radial and circumferential fluctuation velocity components, Ω is the disk rotating speed, and R_d is the radius of the disk. Each plot is the composite of 8 sub-regions.

3.1 Results for the inner configuration

The plots of velocity magnitude on the inter-disk mid-plane are shown in Fig. 8 for 1,000 rpm. The contours and streamlines of air are similar to those of helium. However, in the case of helium (Fig. 8b), the fluid is more affected by the rotation of the disks and the presence of the arm than the air flow (Fig. 8a). For the case of the IC, due to the presence of the arm which occupied half of the space between the disks, the incoming upstream flow is redirected to the narrow space between the arm and the hub. This redirected flow near the hub forms an inverse flow regime rotating in the counterclockwise direction. Since the velocity magnitude of helium is larger than air, the size of the inversed flow of helium is larger than that of air. Most of the incoming flow is redirected to near the hub and the SSU. The streamlines illustrate that helium flow is curved more steeply than in the case of air, and redirected almost parallel to the arm. This redirected flow forms a boundary layer on the body of the arm. The contour plot for helium illustrates

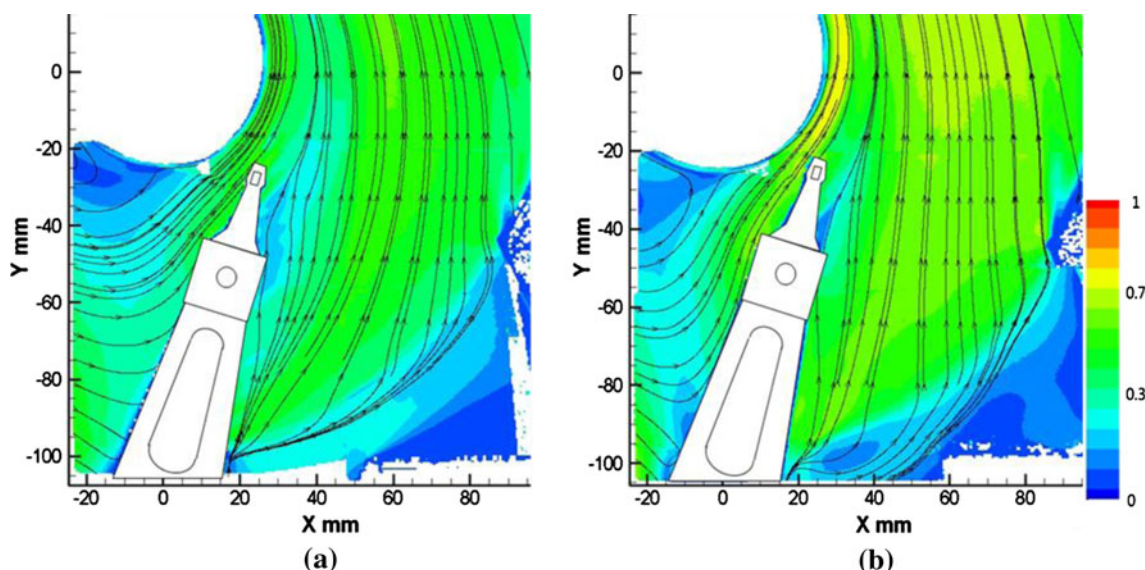


Fig. 8 Mean velocity magnitude of air (a) and helium (b) with streamline at 1,000 rpm (IC)

that the boundary layer flow on the body of the arm is more developed than for air. At the end of the arm, the boundary layer flow is driven through the narrow path between the hub and the SSU. Due to the presence of the stiffening flanges, the flow is extended along the z-axis, and the bulk of flow is redirected again toward the hub. This redirected flow is accelerated by the rotation of the hub. Behind the SSU, significant deceleration is induced by the stiffening flanges on the SSU. Particularly, the helium contour plots show more significant deceleration than the contour plots for air. In the region downstream of the arm, flow influx was found from the outside disk domain for both air and helium due to the presence of the arm (Figs. 8, 9). Since the arm occupies most of the space between the disks, most flow is driven toward the SSU or the outside disk domain. The streamlines superimposed on the contour plots support that most of the flow is driven from the outside disk domain. This driven flow is redirected behind the arm because of the low velocity and low pressure wake region generated by the stiffening flanges. The flow is drawn to the arm for pressure redistribution. The plots of velocity magnitude at 3,000 rpm on the inter-disk mid-plane are shown in Fig. 9. The flow patterns are quite similar to the patterns at 1,000 rpm. However, the helium flow at this rotating speed (Fig. 9b) shows that the redirection of the incoming flow by the presence of the arm is not as steep as that at 1,000 rpm (Fig. 8b). As a result, some of the incoming flow impinges on the body of the arm. Additionally, streamlines of flow influx from the outside rotating frame are not redirected near to the arm as much as for the flow at 1,000 rpm.

The averaged z-axial vorticity plots (Figs. 10, 11) illustrate that highly sheared flows arise due to the presence of the arm and the SSU. In the region upstream of the arm,

near the hub, low positive magnitude of vorticity is observed due to the presence of the flow reversal. Since the size of the flow reversal and the velocity magnitude of helium are larger than those for air, the helium flow (Figs. 10b, 11b) is more intensely sheared near the hub than the air flow (Figs. 10a, 11a). The incoming flow upstream of the arm forms a boundary layer flow up to the stiffening flanges in the SSU. This boundary layer flow induces shear layers as it develops along the body of the arm due to the no-slip boundary condition on the body of the arm. Since the boundary layer of helium is more developed and stronger, the streaks of vorticity for helium display higher magnitudes than those for air on the surface of the arm. Consequently, flow is driven near to the hub and the SSU. The incoming flow driven near to the SSU induces a number of vorticity streaks with alternating signs. The presence of the stiffening flanges contributes to the occurrence of these shear layers. Each corner of the flanges causes a different sign of fluid rotation behind it. Behind the arm, shear layers arise for both air and helium. The flow streaming over the arm is sheared by the presence of the weight saving hole in the middle of the arm. These shear layers are bent toward the hub because the presence of the arm causes a large amount of fluid redirected toward the hub. Since the velocity of the redirected flow of helium is higher than that for air, the shear layers of helium are more curved toward the hub than the shear layers of air. They do not propagated as far as the shear layers of air. At the edge region of the disk, the flow forms a shear layer due to the large velocity gradient between the fixed enclosure wall and the rotating disks.

Most of the turbulence intensity is concentrated toward the downstream of the arm and the SSU, and the edge of

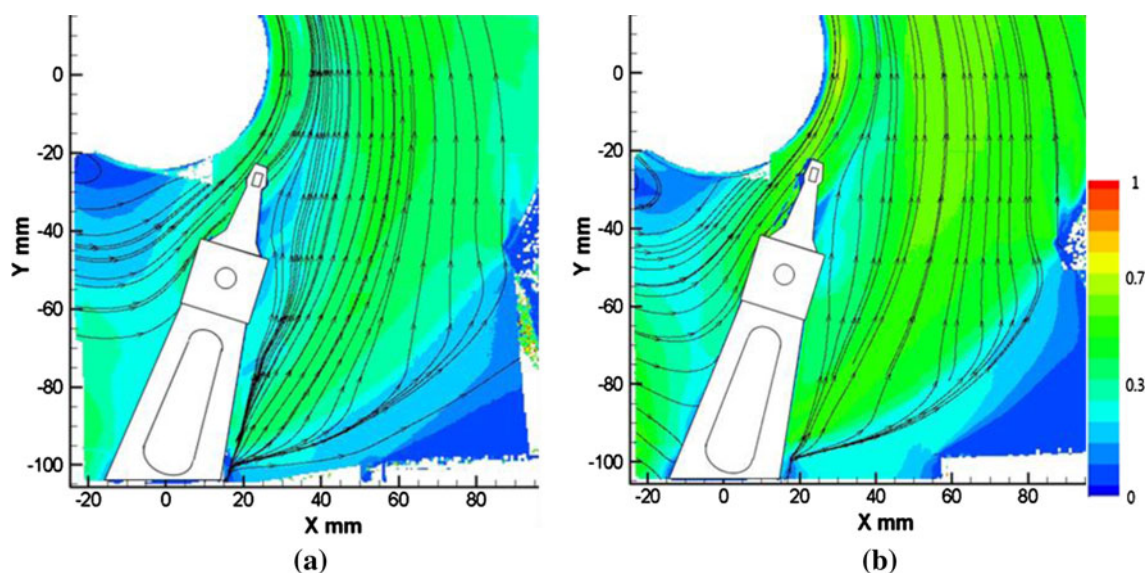


Fig. 9 Mean velocity magnitude of air (a) and helium (b) with streamline at 3,000 rpm (IC)

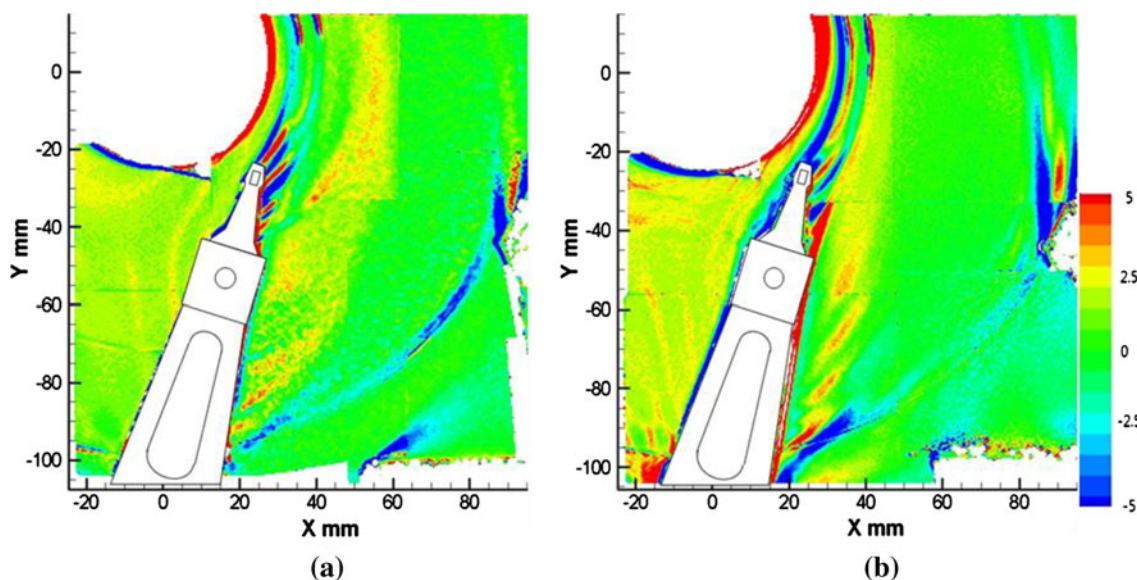


Fig. 10 Plots of mean z-axis vorticity of air (a) and helium (b) at 1,000 rpm (IC)

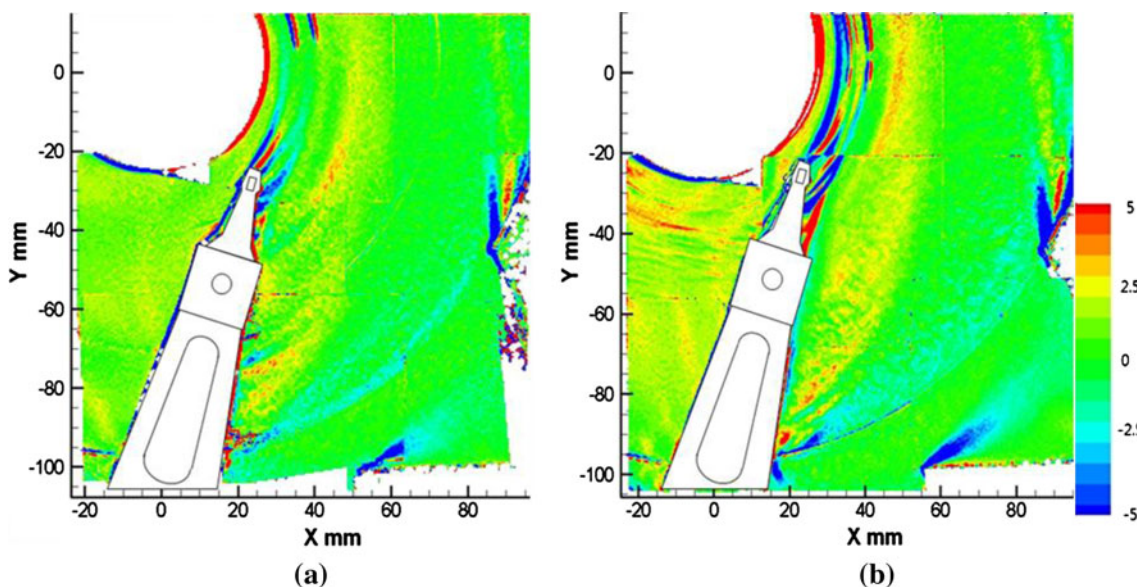


Fig. 11 Plots of mean z-axis vorticity of air (a) and helium (b) at 3,000 rpm (IC)

the disk (Figs. 12, 13). At the inter-disk mid-plane, incoming flow is driven near to the hub and the SSU. This driven flow is perturbed and sheared by the stiffening flanges in the SSU so that the flow becomes three-dimensional and unsteady. Particularly, the stiffening flanges and the weight saving hole in the SSU induce vortex shedding of non-constant frequency behind the SSU. The contour plots of TI^* support the presence of unsteady vortex shedding behind the SSU. Compared to the TI^* of air behind the SSU (Figs. 12a, 13a), the TI^* of helium is smaller (Figs. 12b, 13b). Since the kinematic viscosity of helium is approximately ten times larger than that of air,

the unsteady flow behind SSU dissipates quickly due to the larger relative viscous forces of helium than that for air. This physical phenomenon is supported by the governing equation of turbulence kinetic energy which is defined by:

$$\frac{\partial k}{\partial t} + \underline{U} \cdot \nabla k = -\nabla \cdot \underline{T} + \frac{\underline{\tau}^R : \underline{S}}{\rho} - \varepsilon \tag{4}$$

$$\underline{T} = \frac{1}{2} \underline{u}(\underline{u} \cdot \underline{u}) + \frac{1}{\rho} p' \underline{u} - 2\nu \underline{u} \cdot \underline{\underline{s}} \tag{5}$$

where k is the turbulence kinetic energy, \underline{T} is defined by Eq (5), $\underline{\underline{s}}$ is the mean velocity gradient tensor, \underline{U} is the mean

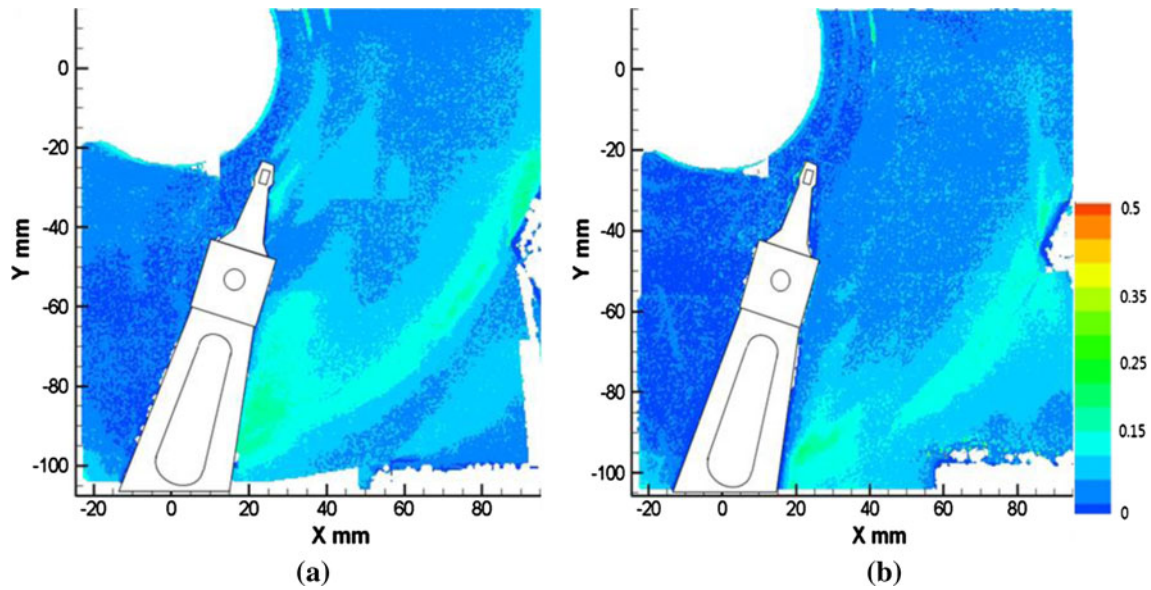


Fig. 12 Turbulence intensity (TI^*) of air (a) and helium (b) at 1,000 rpm (IC)

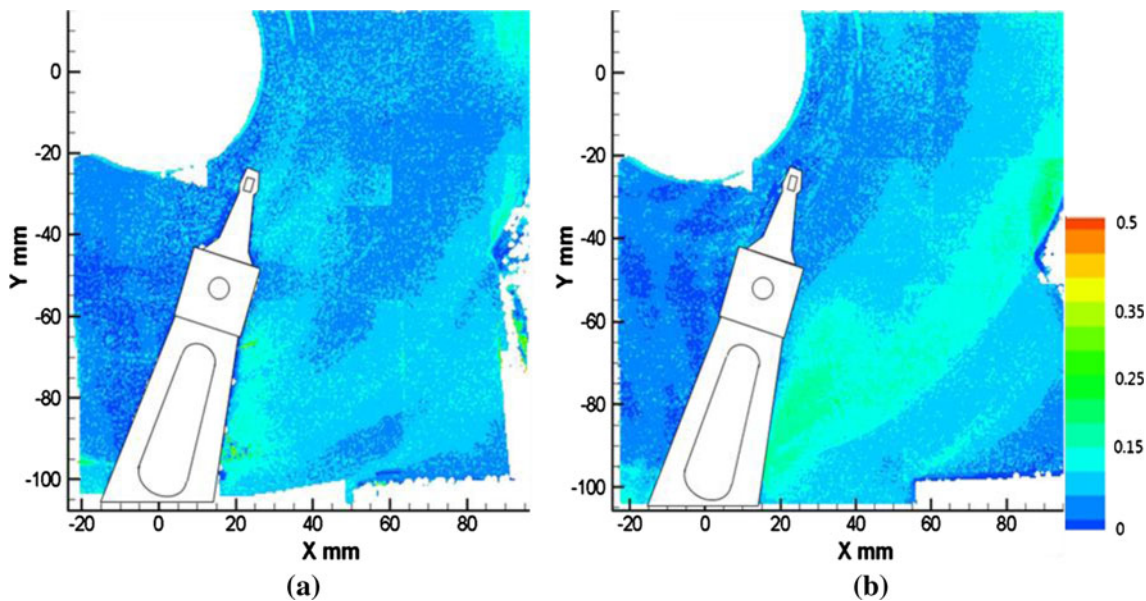


Fig. 13 Turbulence intensity (TI^*) of air (a) and helium (b) at 3,000 rpm (IC)

velocity, \underline{u} is the fluctuating velocity, \underline{s} is the fluctuating tensor velocity gradient tensor, p' is the fluctuating component of the pressure, $\underline{\tau}^R$ is the Reynolds stress tensor, and ε is the dissipation of k . In dimensionless form, this equation is given by

$$\frac{\partial k^*}{\partial t} + \underline{U}^* \cdot \nabla k^* = -\nabla \cdot \underline{T}^* + \underline{\tau}^{R*} : \underline{S} - \frac{1}{\text{Re}} \varepsilon^* \quad (6)$$

where $*$ indicates non-dimensionalization and Re is LV/v , L and V with the characteristic length and velocity

scales. At respectively constant rotating speed, the Re of helium is always smaller than that of air. Therefore, in general, the helium flow has a higher absolute value of normalized dissipation than the flow of air, which works to dampen the velocity fluctuations in helium more than in air.

3.2 Results for the outer configuration

The contour plots of velocity magnitude with streamlines at 1,000 rpm are shown in Fig. 14. The streamlines illustrate

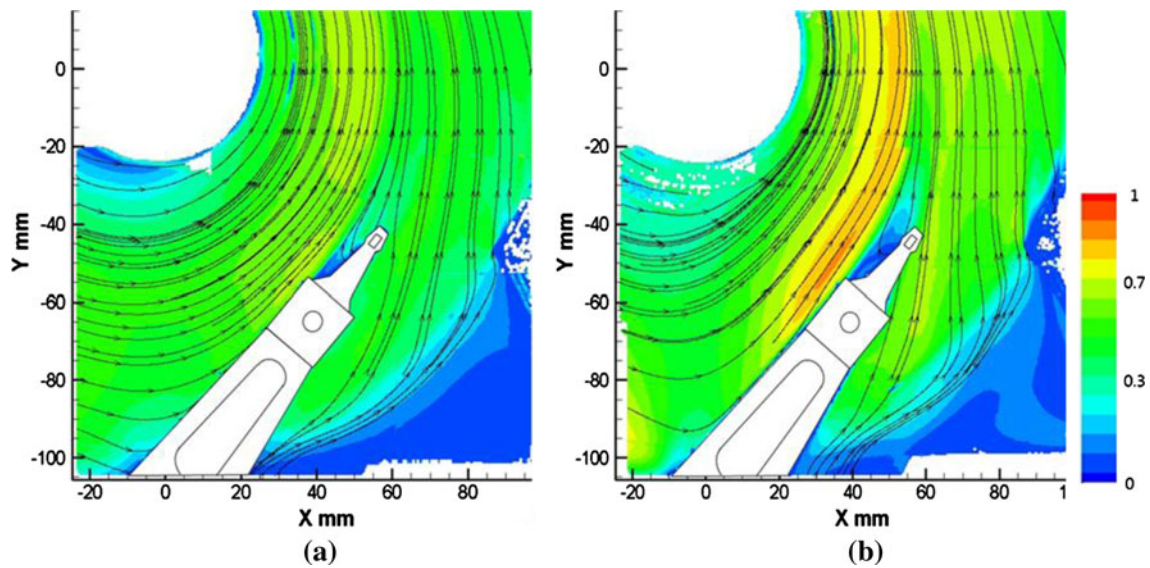


Fig. 14 Mean velocity magnitude of air (a) and helium (b) with streamline at 1,000 rpm (OC)

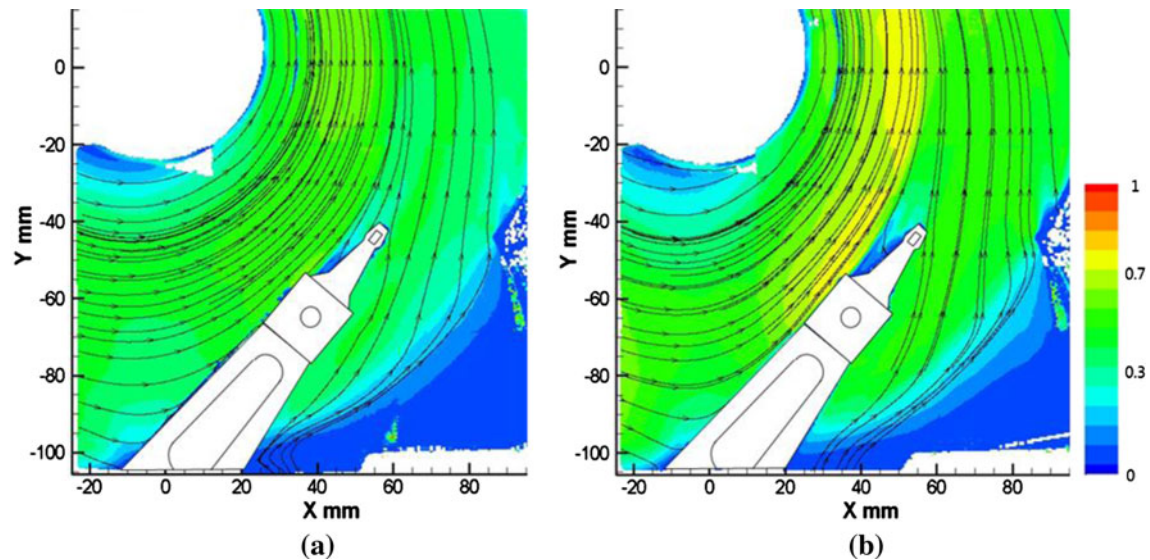


Fig. 15 Mean velocity magnitude of air (a) and helium (b) with streamline at 3,000 rpm (OC)

that most of the incoming flow is redirected toward the rotating hub. Since the space between the arm and the hub is more opened than that of the IC, the presence of the inverse flow upstream of the arm is not observed. At the same time, this redirected flow forms a stronger boundary layer flow on the lateral surface of the arm. At the end of the arm, more developed boundary layer flow is observed. For the case of the helium flow (Fig. 14b), a higher velocity magnitude than that of air (Fig. 14a) is observed. Since the direction of the redirected flow is almost parallel to the direction of the arm, the fluid region between the upper and the lower SSU forms a low velocity region which is almost not affected by the incoming flow and the

rotation of the disks. Behind the arm, streamlines support that most of flow is redirected from the outside rotating frame. The two streams join near the region downstream of the SSU. The flow pattern at 3,000 rpm (Fig. 15) is similar to the pattern at 1,000 rpm. Also similar to the flow pattern for the IC, the redirection of the incoming flow upstream of the arm in the helium flow (Fig. 15b) is less severe than that at 1,000 rpm (Fig. 15a). Moreover, the redirected flow from the outside rotating frame is not pulled as strongly into the SSU at 3,000 rpm.

The contour plots of average z-axial vorticity are shown in Figs. 16 and 17. For both air and helium, the incoming flow is strongly sheared on the body of the arm. The incoming flow

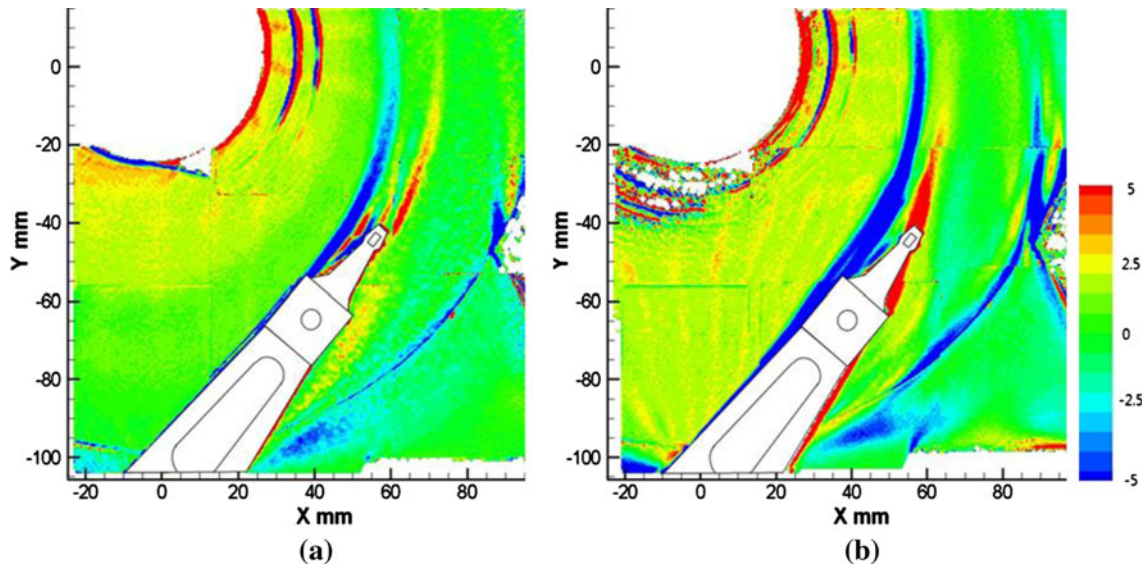


Fig. 16 Plots of Z-axial vorticity of air (a) and helium (b) at 1,000 rpm (OC)

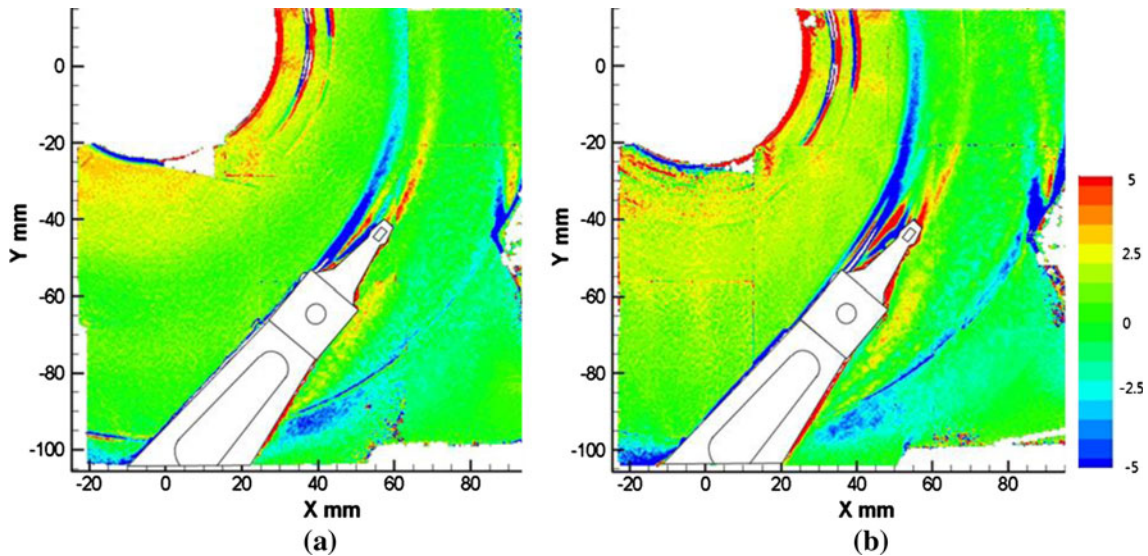


Fig. 17 Plots of Z-axial vorticity of air (a) and helium (b) at 3,000 rpm (OC)

forms a boundary layer flow on the body of the arm. This flow is sheared by the stiffening flanges as well as low velocity region between the upper and the lower SSU. This vorticity trail of the helium flow (Figs. 16b, 17b) appears to be longer and more intense than that of the air flow (Figs. 16a, 17a). The higher kinematic viscosity of helium contributes to induce more intense vorticity trails on the body of the arm compared with air. Additionally, some weak vorticity streaks are found in the space between the arm and hub for the case of the helium flow (Figs. 16b, 17b). These vorticity streaks are generated by the sudden direction change of the incoming flow by the arm. Since the incoming flow of the air flow is not redirected as steeply as the helium flow, these weak vorticity

streaks are not observed in the air flow (Figs. 16a, 17a). Behind the arm and SSU, a positive vorticity trail is induced. This vorticity trail is caused by large velocity gradients generated by the edge of the arm and the stiffening flanges on the SSU while fluid is redirected toward the rotating hub. Similar to the IC, at the edge of the disk region, the flow forms a shear layer due to the large velocity gradient between the inside rotating frame and the outer enclosure. At 3,000 rpm, the pattern of shear layer generation (Fig. 17) is almost identical to the shear layer pattern at 1,000 rpm. However, the fluid appears to have a lower non-dimensionalized magnitude of z-axial vorticity compared to that at 1,000 rpm.

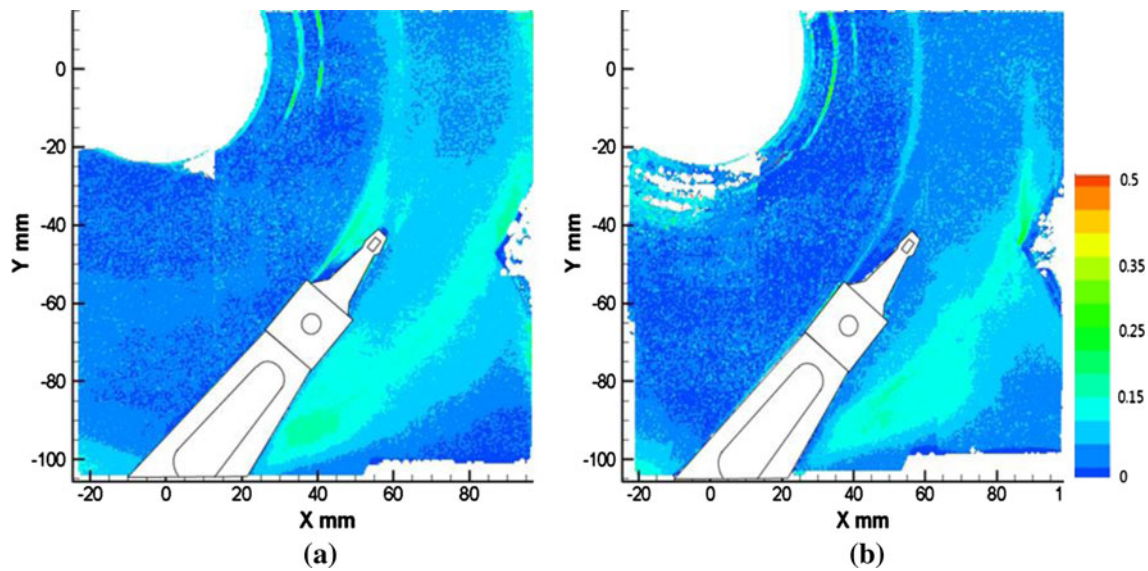


Fig. 18 Turbulence intensity (TI^*) of air (a) and helium (b) at 1,000 rpm (OC)

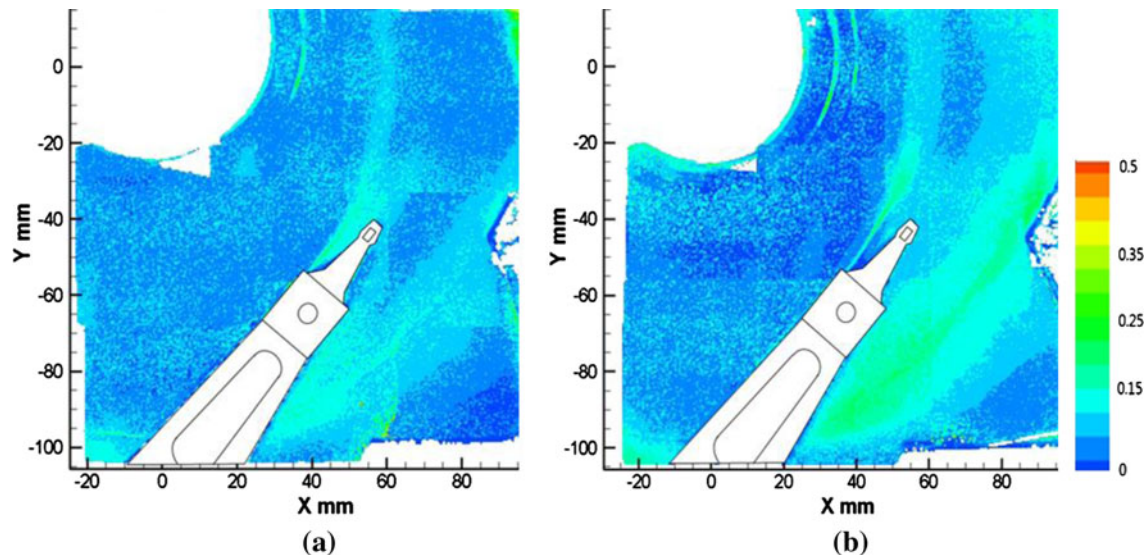


Fig. 19 Turbulence intensity (TI^*) of air (a) and helium (b) at 3,000 rpm (OC)

Similar to the flow for the IC, contour plot of the TI^* at 1,000 and 3,000 rpm (Figs. 18, 19) reveals that most of the TI^* is concentrated in the region near the SSU and the edge of the disk. Since the space between the hub and the arm is opened more than for the IC, an inner region with low magnitude of TI^* is observed in the unobstructed flow. However, the boundary layer flow on the arm formed by incoming flow induces turbulence with high magnitude at the end of the arm where shear layer generates. This turbulence is strengthened near the SSU and dissipated gradually along the rotation direction. As with the IC case, the higher viscous force of helium (Figs. 18b, 19b) reduces the magnitude of turbulence near the SSU more than the air

flow (Figs. 18a, 19a). Behind the weight saving hole, unsteady vortex shedding is induced. This region overlaps with a shear layer region at the edge of the disk. As a result, TI^* with high magnitude arise in this region and it gradually fades along the edge of the disk, but this has little effect on the SSU and its positioning accuracy. The main reason is the large mass of the E-block and the arm.

4 Conclusions

PIV measurements have been performed at the inter-disk mid-plane around the arm and the SSU of the model hard

disk drive. The results reveal different nature of fluid–structure interaction phenomena for air-filled and helium-filled drive. The different characteristics of the air and the helium flow can be summarized by (1) The helium flow is more accelerated by the rotation of the disk and decelerated by the presence of the arm and the SSU than the air flow. (2) The higher kinematic viscosity of helium induces longer and intensified vorticity trails downstream of the arm and the SSU than air. (3) The magnitude of Tl^* in the helium flow around the SSU appears to be much lower than that of the air flow at both rotating speeds. The lower turbulence intensity level around the SSU is expected to reduce flow-induced vibration on the SSU and increase positioning accuracy.

Acknowledgments The author acknowledges financial support by INSIC (Information Storage Industry Consortium). for his master's studies. SK and HH-H express their gratitude to Joseph A.C. Humphrey for his conception of the ideas underpinning this work. Professor Humphrey passed away prior to completion of this work.

Conflict of interest The authors declare that they have no conflict of interest.

References

- Abrahamson SD, Koga DJ, Eaton JK (1988) The flow between shrouded co-rotating disks. *Phys Fluids* 11(2):241–251
- Aruga K, Suwa M, Shimizu K, Watanaba T (2007) A study on positioning error caused by flow induced vibration using helium-filled hard disk drives. *IEEE Trans Magn* 43(9):3750–3755
- Barbier C (2006) Experimental and numerical study of the flow in a simulated hard disk drive. PhD thesis, University of Virginia, Department of Mechanical and Aerospace Engineering
- Barbier C, Humphrey JAC, Maslen E (2006) Experimental study of the flow in a simulated hard disk drive. *J Fluid Eng* 128:1–11
- Coughlin TM (2001) High density hard disk drive trends in the USA. *J Magn Soc Japan* 25(3):111–120
- Davidson PA (2004) *Turbulence. An introduction for scientists and engineers*. Oxford University Press, USA
- Hirono Y, Arisaka T, Nishijima N, Shimizu T, Nakamura S, Masuda H (2004) Flow-induced vibration reduction in HDD by using a spoiler. *IEEE Trans Magn* 40(4):3168–3170
- Ikegawa M, Hirono Y, Mukai H, Kaiho M (2006) Decreasing airflow velocity in hard disk drives with a spoiler and bypass. *IEEE Trans Magn* 42(10):2594–2596
- Kaneko S, Nishihara T, Watanabe T (2007) Aerodynamic characteristics of carriage arm equipped on hard magnetic disks. *Microsyst Technol* 13:1297–1306
- Kazemi K (2008) Analysis of the slider off-track vibration caused by the aerodynamic loads associated with different components of a head stack assembly in a disk drive. *IEEE Trans Magn* 44(5):633–639
- Kazemi K (2009) Investigation of fluid structure interaction of a head stack assembly in a hard disk drive. *IEEE Trans Magn* 45(12):5344–5351
- Keane RD, Adrian RJ (1990) Optimization of particle image velocimeters. Part I: double pulsed system. *Meas Sci Technol* 1:1202–1215
- Lennemann E (1974) Aerodynamics aspect of disk files. *IBM J Res Dev* 18:480–488
- Nakamura S, Aduma R, Takahashi H, Wakatsuki K, Hagiya S (2005) Flow-induced vibration of a head gimbal assembly under various conditions. *IEEE Trans Magn* 41(2):769–773
- Shimizu H, Shimizu T, Tokuyama M, Masuda H, Nakamura S (2003) Numerical simulation of positioning error caused by air-flow-induced vibration of head gimbals assembly in hard disk drive. *IEEE Trans Magn* 39(2):806–811
- Tatewaki M, Tsuda N, Maruyama T (2001) An analysis of disk flutter in hard disk drives in aerodynamic simulations. *IEEE Trans Magn* 37(2):842–846
- Tzeng H-M, Humphrey JAC (1991) Co-rotating disk flow in an axisymmetric enclosure with and without bluffing body. *Int J Heat Fluid Flow* 12(3):194–201
- Usry WR, Humphrey JAC, Greif R (1993) Unsteady flow in the obstructed space between disks corotating in a cylindrical enclosure. *J Fluid Eng* 115:620–626
- Wood R (2008) Future hard disk drive systems. *J Magn Magn Mater* 321(6):555–561
- Zhang QD, Tan CS, Sundaravadivelu K, Suriadi MA, Chin GL, Yip TH, Ong EH, Liu NY (2010) Mitigation of flow induced vibration of head gimbal assembly. *Microsyst Technol* 16:213–219